

## Effect of Dissolved Oxygen on Pitting Corrosion Behavior of Low-Alloy Steel under Hydrostatic Pressure

Hongyi Su, Yi Liang, Yujiang Wang, Bo Wang, Hui Tong, Yue Yuan, Shicheng Wei\*

National Key Laboratory for Remanufacturing, Army Academy of Armored Forces, Beijing 100072, PR China

\*E-mail: [wsc33333@163.com](mailto:wsc33333@163.com)

\*E-mail: [liangyi365@126.com](mailto:liangyi365@126.com)

Received: 28 January 2019 / Accepted: 11 March 2019 / Published: 10 April 2019

---

Effect of dissolved oxygen on pitting corrosion behavior of low-alloy steel under hydrostatic pressure in neutral 3.5 wt.% NaCl solution was investigated by scanning electron microscope (SEM), 3-D measuring microscope and so on. The results show that the combined effect of hydrostatic pressure and dissolved oxygen increases the overall growing rate of corrosion pits and causes deeper corrosion pits but decreases their sizes in the horizontal direction. Electrochemical measurement results reveal that dissolved oxygen dominates the corrosion kinetics of low-alloy steel in the environment containing high hydrostatic pressure and high dissolved oxygen by accelerating cathodic process, slowing down the anodic process and promoting open circuit potential (OCP). Consequently, the increased charge transfer process makes the pits have a larger volume and depth. Meanwhile, the decreased initial potential energy difference based on energy theory calculation at the initiation site by dissolved oxygen possibly inhibits the pitting growth in the horizontal direction.

---

**Keywords:** Low-alloy steel; Combined effect; Pitting corrosion; Theoretical calculation

### 1. INTRODUCTION

Nowadays, the scientific activities for the mysterious deep sea are proceeding at a high rate. These works depend on the deep-sea devices such as underwater robot, submersible and so on. The devices made of metal materials are immersed in deep-sea water day and night, suffering severe corrosion. Once corroded, their mechanical performances will be greatly degraded. Therefore, the corrosion problems in deep-sea environment have gathered extensive concern of many scientific researchers. There are various factors that can affect the corrosion behavior of metals in deep-sea environment. Among them, hydrostatic pressure is a unique factor, which increases 1atm per 10m in depth. In the past several decades, the effect of hydrostatic pressure on metal corrosion is always a focus

1. Beccaria [6, 7] is one of the researchers firstly engaging in this aspect of study. The main results can be described that hydrostatic pressure accelerates the localized corrosion of aluminum and its alloys, leading to deeper corrosion pits. An investigation provided by Zhang, et al. 8 reveals that hydrostatic pressure degrades the pitting resistance of 316L stainless steel by decreasing Fe(III)/Fe(II) ratio, Cr(III)-oxides as well as structural inhomogeneity of the passive films. However, these experimental results from laboratory can neither apply nor well explain the corrosion phenomena in deep-sea environment because dissolved oxygen as a significant factor for corrosion also changes evidently with water depth. Therefore, studying the combined effect of hydrostatic pressure and dissolved oxygen on the corrosion behavior of metals is needed to distinguish the corrosion phenomena in deep-sea environment.

Low-alloy steels are widely used for marine structures owing to excellent mechanical properties and good weldability. Unlike stainless steels, these steels show quite different localized corrosion behaviors at hydrostatic pressure including pit morphology, formation kinetics and mechanism. The main point about hydrostatic pressure effect on the corrosion of low-alloy steel can be described that hydrostatic pressure can accelerate the interaction between metal matrix and  $\text{Cl}^-$ , the pitting propagation in 3D direction, and the transform from pit corrosion to uniform corrosion 9. This point is convincing as hydrostatic pressure is the unique variable. But under the condition that hydrostatic pressure is combined with dissolved oxygen, the corrosion mechanism of low-alloy steel are not readily understood. Hence, doing this part of work will benefit the understanding of corrosion phenomena in deep-sea environment and material design.

In our report, the combined effect of hydrostatic pressure and dissolved oxygen on the pitting corrosion of low-alloy steel in neutral 3.5 wt.% NaCl solution is investigated. One interesting phenomenon is found in our work that these two combined factors accelerate the growth of pits in the depth direction, meanwhile inhibit their propagation in the horizontal direction. More detailed work was carried out to explain this phenomenon.

## 2. EXPERIMENTAL METHOD

### 2.1 Material and solution

A hot rolled plate of low-alloy steel was used as test samples. The composition of it is shown in Table 1. The samples cut into a size of 20 mm × 20 mm × 4 mm were used for morphology observations. The samples cut into a size of 10 mm × 10 mm × 4 mm for electrochemical measurements were embedded in epoxy resin, leaving an open area of 1 cm<sup>2</sup>. All the samples were ground to 2400 grit-finish, polished with 2 μm diamond polishing film, and then cleaned with distilled water and acetone before test. The testing environment was a neutral 3.5 wt.% NaCl solution at room temperature (25±1 °C).

**Table 1.** Chemical composition of the studied low-alloy steel (wt.%)

Element	C	Si	Mn	Cr	Ni	Mo	V	Fe
Mass %	0.1	0.29	0.57	0.6	4.96	0.6	0.09	Bal.

## 2.2 Experimental equipment

Schematic diagram of the experimental setup is presented in Fig. 1. It consists of pressure vessel, pneumatic liquid booster pump, temperature control and dissolved oxygen control system. As the experimental setup works, the pneumatic liquid booster pump connected to the air pump pushes the aqueous solution into the pressure vessel through high pressure ventilation generated by the air pump. The increased aqueous solution can compress the remaining gas in pressure vessel and hydrostatic pressure can be obtained. To investigate the combined effect of hydrostatic pressure and dissolved oxygen on the corrosion behavior of steel, it is necessary to ensure that these two factors change at the same time. One of the simple methods is using air as pressurization gas. According to Henry's Law, as the hydrostatic pressure increases, the dissolved oxygen concentration increases linearly, and the hydrostatic pressure and dissolved oxygen concentration can be identified under various conditions. In this study, as the hydrostatic pressure increases from 1 atm to 60 atm, the concentration of dissolved oxygen correspondingly increases from  $2.7 \times 10^{-4}$  mol/L to  $1.6 \times 10^{-2}$  mol/L. The test condition at atmospheric pressure is denoted as AP and the combined condition at high hydrostatic pressure and high dissolved oxygen is denoted as HPO.

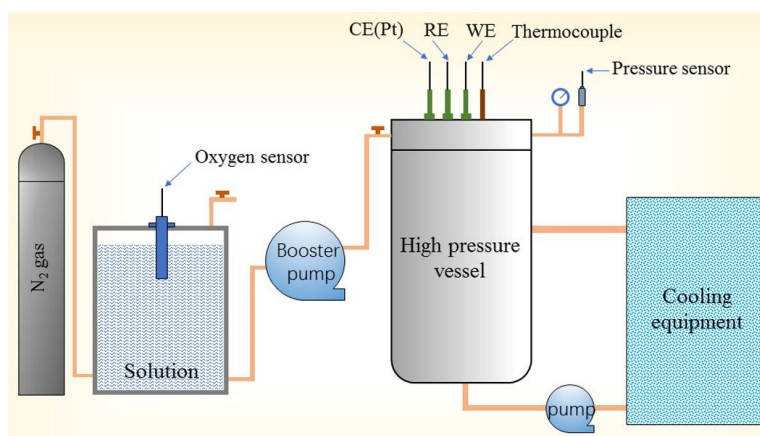


**Figure 1.** Schematic diagram of the experimental setup.

## 2.3 Electrochemical measurement

Potentiodynamic polarization measurements were conducted using a conventional three-electrode system. The steel sample was used as the working electrode, Pt plate as the counter electrode and Ag/AgCl as the reference electrode. The potential scanning rate was 1mV/s from the initial potential of -800mV to the ultimate potential of 200 mV before a stable OCP was established within 1h.

Electrochemical impedance spectroscopy (EIS) measurements were performed after the OCP is stable. The test frequency range is from 100kHz to 10mHz, with 10 mV perturbation versus OCP. The obtained results were interpreted by using fitting software ZsimpWin software.

## 2.4 Morphology observations

The metallographic structure of the low-alloy steel was observed by optical microscope. The

macroscopic appearance of the corroded samples was observed by digital camera. The microscopic images of the inclusion and corrosion pits on the low-alloy steel after test were measured by SEM combined with Energy Disperse Spectroscopy (EDS). The 3D sizes of corrosion pits were measured by confocal scanning laser microscope (OLYMPUS OLS4000) after removing corrosion products by hexamethylenetetramine contained hydrochloric acid solution.

### 3. RESULTS AND DISCUSSION

#### 3.1 Microstructure

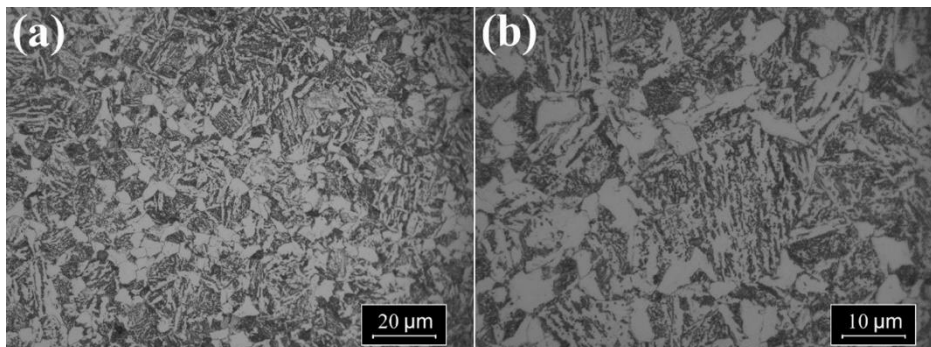


**Figure 2.** The metallographic structure of the low-alloy steel.

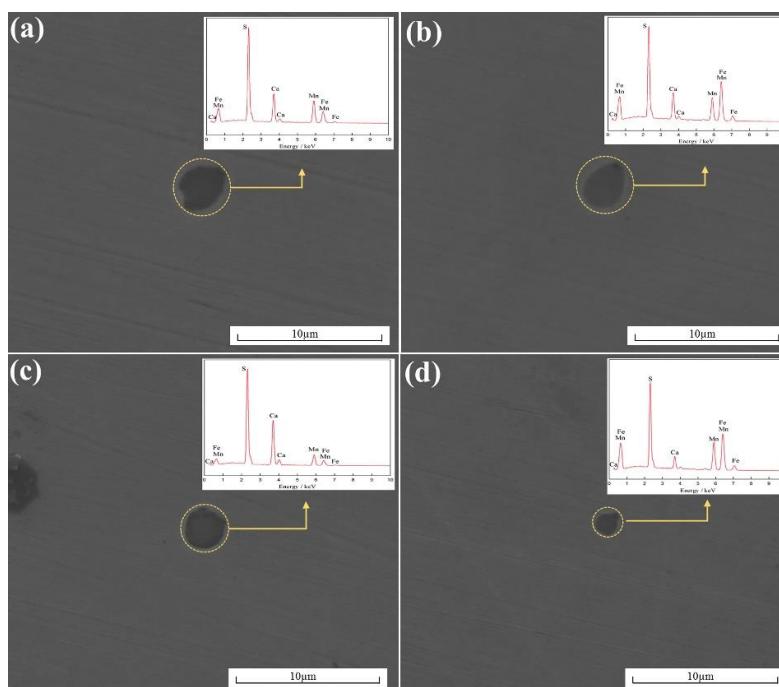


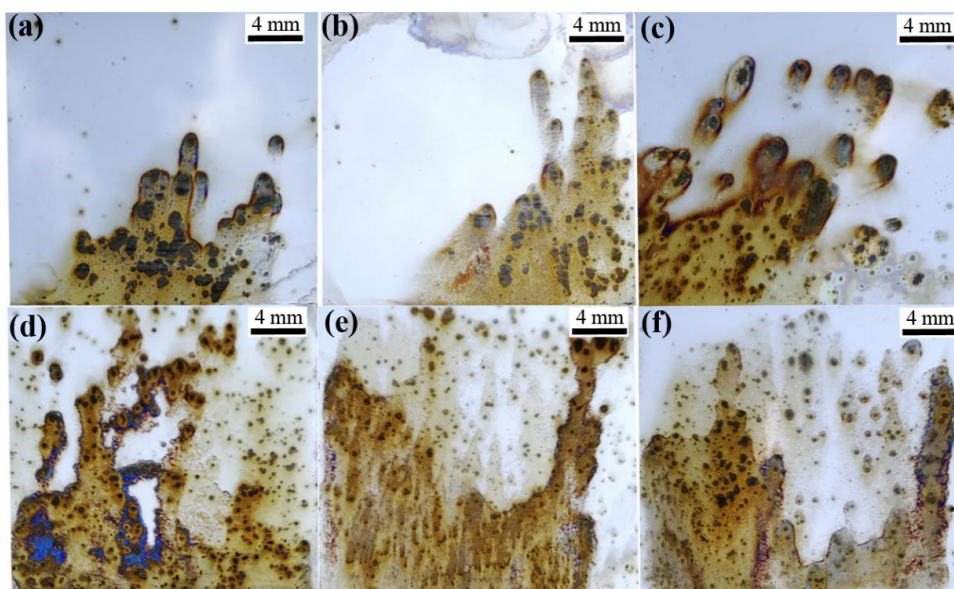
**Figure 3.** SEM and EDS analysis of inclusions within the low-alloy steel sample:(a), (b), (c) and (d) inclusions at different locations, respectively.

The metallographic structures of the low-alloy steel are shown in Fig. 2. There are two different kinds of morphologies, parallel bainite and polygonal ferrite. Fig. 3 shows the morphologies of some

typical inclusions on steel surface. The dark regions in the picture are the typical inclusions. EDS results reveal that the inclusions are the compounds of Mn-Ca-S 12. , which present a spherical shape (Fig. 3a, Fig. 3b and Fig. 3c) or polygonal shape (Fig. 3d)13. In general, the inclusions have a size of several microns.

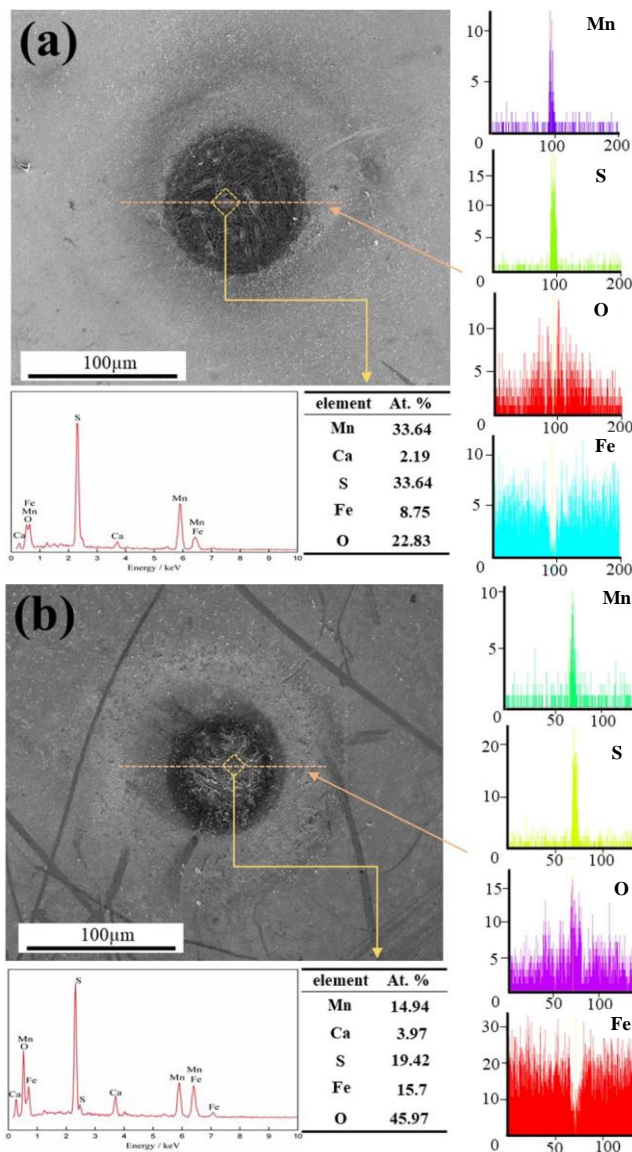
### 3.2 Pit observation

The macroscopic corrosion morphologies of the low-alloy steel tested at AP and HPO after 6h immersion were shown in Fig. 4. The dark spots in picture are the localized corrosion regions and their formation is associated with the enlargement or the coalescence of pits. The brown areas are the cathode regions. Notably, the amounts, sizes and distribution patterns of the dark spots at HPO are different with AP. The number of the megascopic dark spots formed at HPO are more than AP, however, most of them formed at HPO have smaller sizes than AP. Additionally, the dark spots occur nearly on the entire surface at HPO while take place at localized areas at AP. It indicates that HPO stimulates the generation of corrosion pits but inhibits their propagation in the horizontal direction or their coalescence.



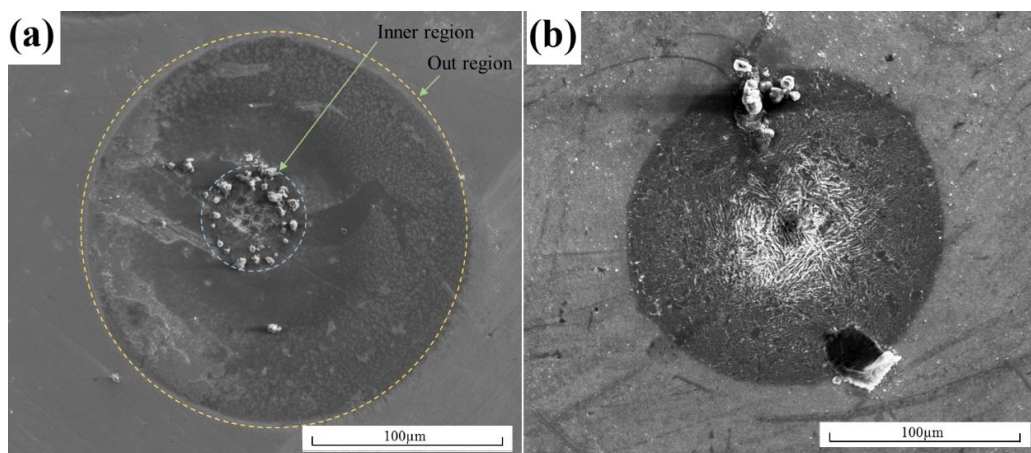
**Figure 4.** The macroscopic corrosion morphologies of low-alloy steel after 6h immersion in neutral 3.5 wt.% NaCl solution: (a), (b), (c) at AP; (d), (e), (f) at HPO.

SEM images of the corrosion pits for low-alloy steel formed at AP and HPO after 6h immersion are shown in Fig. 5. Pits form at inclusions both at AP and HPO. EDS results reveal that the initiation sites are both the compounds of Mn-Ca-S. It seems that the corrosion pits initiate at the junction of inclusion and substrate 16, as shown in Fig. 5(a). Due to the chemical inhomogeneity, these zones usually have high dissolved activity and could be the initiation sites of corrosion pits. In Fig. 5(b), the inclusion in pit at HPO is not readily distinguished in the picture. EDS results reveal that the inclusion site might be covered with corrosion products.

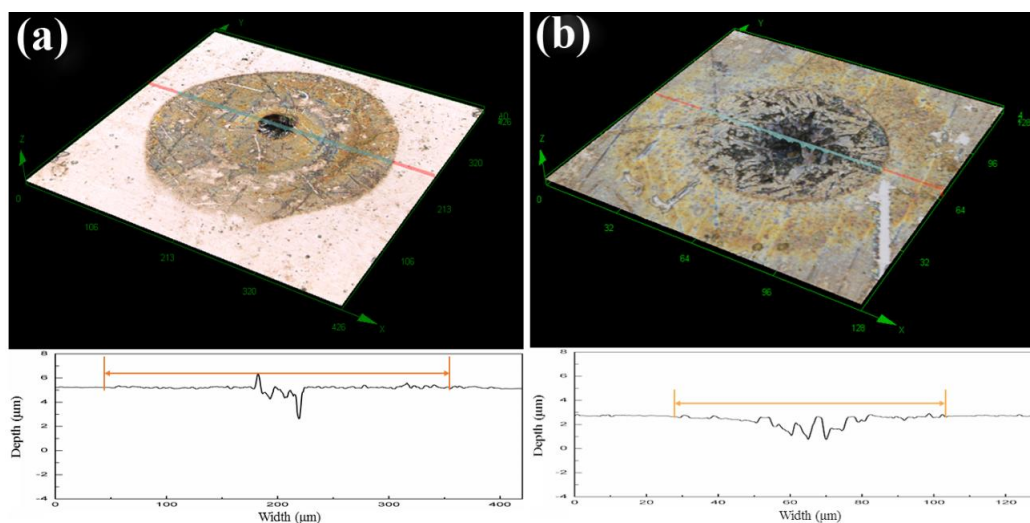


**Figure 5.** The microscopic morphologies of the corrosion pits on low-alloy steel samples after 6h immersion in neutral 3.5 wt.% NaCl solution: (a) at AP, (b) at HPO.

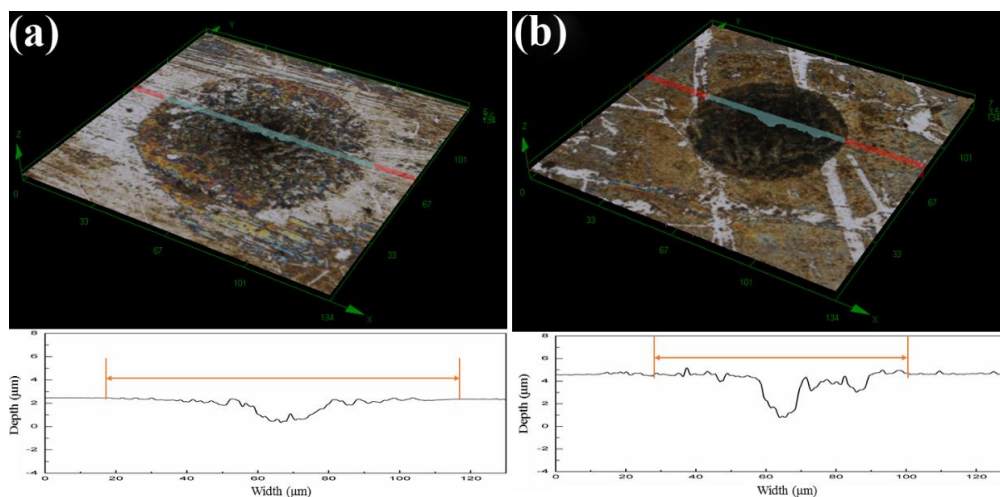
low-alloy steelThe microscopic morphologies of the corrosion pits on low-alloy steel at AP and HPO after 0.5h immersion are shown in Fig. 6. The corrosion pits at AP are composed of an inner circular region and an outer annulus region, as shown in Fig. 6(a). The inner circular region exhibits a fold shape and the outer annulus region shows a smoother morphology, indicating that the two regions are formed in different immersion stages. However, the boundary of corrosion pits between the inner circular region and the outer annulus region is not easily distinguished for HPO, as shown in Fig. 6(b). Combined with Fig. 5, it can be speculated that the pitting morphology in Fig. 6(a) forms in the preliminary step of pit growth. With the growth of pit, the smoother outer annulus changes to fold-like morphology and the boundary between the inner circular region and the outer annulus region fades away, as shown in Fig. 6(b). Therefore, it can be demonstrated that HPO accelerates the growth of corrosion pits.



**Figure 6.** The microscopic morphologies of the corrosion pits on low-alloy steel sample after 0.5h immersion in neutral 3.5 wt.% NaCl solution: (a) at AP, (b) at HPO.



**Figure 7.** 3D images of corrosion pits on low-alloy steel samples after 0.5h immersion in neutral 3.5 wt.% NaCl solution: (a) at AP, (b) at HPO.



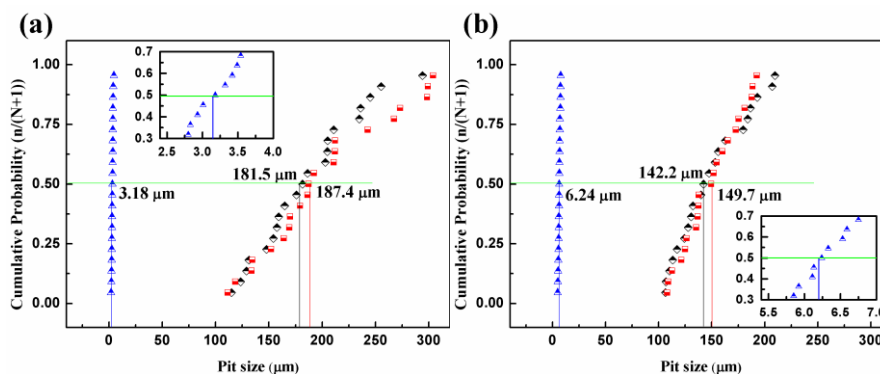
**Figure 8.** 3D images of corrosion pits on low-alloy steel samples after 6h immersion in neutral 3.5 wt.% NaCl solution: (a) at AP, (b) at HPO.

Fig. 7 and Fig. 8 respectively display the 3D images of the corrosion pits after 0.5h and 6h immersion. Apparently, the corrosion pits formed at HPO have a rougher morphology and a more rugged cross-sectional profile than at AP both for 0.5h and 6h immersion. It indicates that HPO accelerates the pitting growth in the depth direction. However, the sizes of corrosion pits in the horizontal direction formed at HPO are smaller than that at AP both for 0.5h and 6h immersion, implying that HPO inhibits the horizontal propagation of pits.

### 3.3 Pit sizes

Statistical distribution results of the three-dimensional sizes for corrosion pits formed at AP and HPO after 3h immersion are shown in Fig. 9. The mean rank method is used to calculate the cumulative probability, denoted as  $n/(N+1)$ , of the pitting geometry parameters including length, width and depth. Here,  $n$  is the order in the total number of pits and  $N$  is the total number. The value in the position where cumulative probability  $P=0.5$  expresses the typical sizes of corrosion pits.

In Fig. 9, the average diameters of the corrosion pits in the length direction and width direction for HPO are 149.7  $\mu\text{m}$  and 142.2  $\mu\text{m}$  respectively, which are both smaller than that at AP with 187.4  $\mu\text{m}$  and 181.5  $\mu\text{m}$ . It means that HPO inhibit the horizontal propagation of corrosion pits. The depth of corrosion pits at HPO with 6.24  $\mu\text{m}$  is bigger than that at AP with 3.18  $\mu\text{m}$ , indicating that HPO increases the depth of corrosion pits.



**Figure 9.** Statistical distributions results of the 3D sizes of corrosion pits at different testing conditions after 6h immersion in neutral 3.5 wt.% NaCl solution: (a) at AP, (b) at HPO.

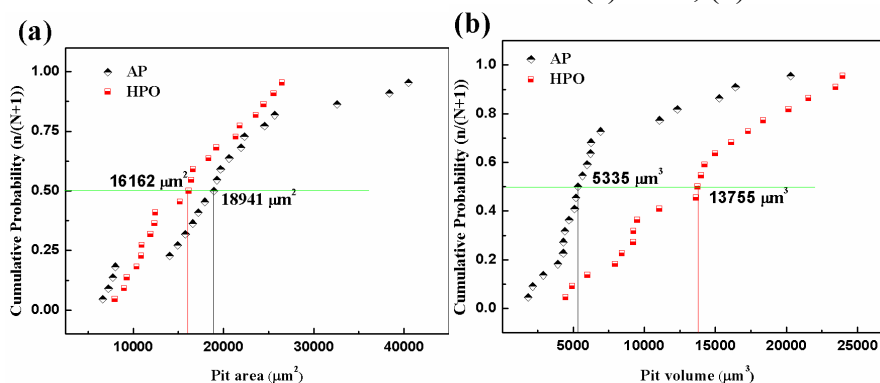


**Figure 10.** Statistical distributions results of the superficial area and the volume of pits obtained at AP and HPO in neutral 3.5 wt.% NaCl solution: (a) superficial area, (b) volume.

The cumulative probability results of the superficial area and the volume of the pits formed at AP and HPO respectively are shown in Fig. 10. It can be figured out that the average superficial area of the pits at HPO with  $16162 \mu\text{m}^2$  is smaller than that at AP with  $18941 \mu\text{m}^2$  but the average volume of pits at HPO with  $13755 \mu\text{m}^3$  is much bigger than that at AP with  $5335 \mu\text{m}^3$ . It indicates that HPO accelerates the overall growing rate of corrosion pit but inhibits their growth in the horizontal direction.

### 3.4 Electrochemical measurements

The experimental results above reveal that HPO inhibits the growth of corrosion pits in the horizontal direction, however, accelerates their growth in the depth direction and the overall growing rate. This conclusion is different with that obtained by Yang, et al. 11 Their study shows that as hydrostatic pressure is the only variable, it accelerates the growth of pits for low-alloy steel in 3.5 NaCl solution both in the horizontal and depth direction. It should be noted that the dissolved oxygen concentration has a low level in the tests. Hence, it indicates that the main factor that causes the different experimental results could be the dissolved oxygen. In order to demonstrate this opinion, the potentiodynamic polarization tests were conducted and the results are shown in Fig. 11. Yang, et al. 10 have found that hydrostatic pressure increases the anodic reaction rate of the steel due to the increased activity of  $\text{Cl}^-$  but does not change the cathodic reaction as hydrostatic pressure is a single factor. As a result, hydrostatic pressure decreases the corrosion potential of low-alloy steel. However, in the combined environment containing high hydrostatic pressure and high dissolved oxygen, the cathodic reaction process is accelerated but the anodic process is inhibited. Hence, the corrosion potential of low-alloy steel shifts in the positive direction. It is well established that the increase of dissolved oxygen concentration can increase the cathodic reaction rate and promote OCP. Therefore, it is possible that the corrosion kinetics of the steel is mainly dominated by dissolved oxygen in the combined environment. To confirm the leading role of dissolved oxygen in the corrosion process, OCP tests were conducted both at AP and HPO and the results are presented in Fig. 12. It is obvious that the OCP at HPO is more notable than at AP, which supports our opinion.

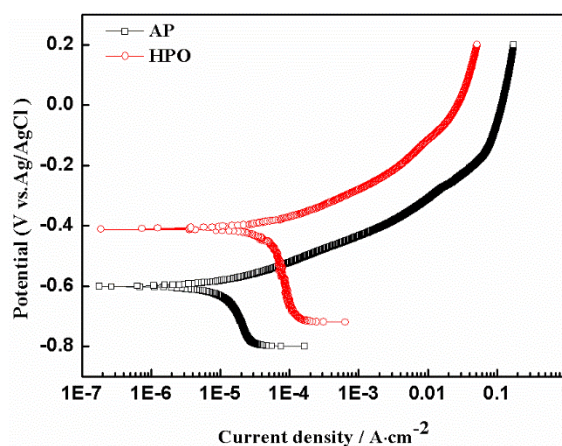


**Figure 11.** The potentiodynamic polarization curves of low-alloy steel tested at AP and HPO in neutral 3.5 wt.% NaCl solution.

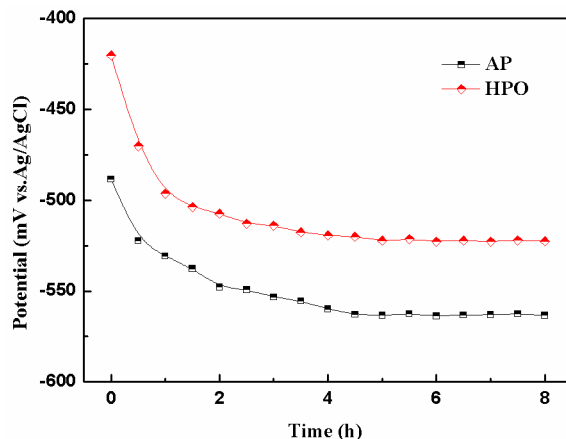


**Figure 12.** OCP evolution with time for low-alloy steel at AP and HPO in neutral 3.5 wt.% NaCl solution .

Tafel extrapolation method is used to analyze the potentiodynamic polarization curves and the fitted results are shown in Table 2. It is seen that both cathodic Tafel constant,  $b_c$ , and anodic Tafel constant,  $b_a$ , for AP have a similar value with the ones for HPO. It indicates that the corrosion mechanism of low-alloy steel is not changed by HPO 24. Additionally, the corrosion current density for HPO is much higher than the one for AP.

**Table 2.** The fitted results of potentiodynamic polarization curves for low-alloy steel.

Condition	$E_{corr}$ (mV)	$i_{corr}$ A cm <sup>-2</sup>	$b_a$ mV/dec	$b_c$ mV/dec
AP	-0.608	4.75	66.4	-258
HPO	-0.448	38.3	65.3	-279

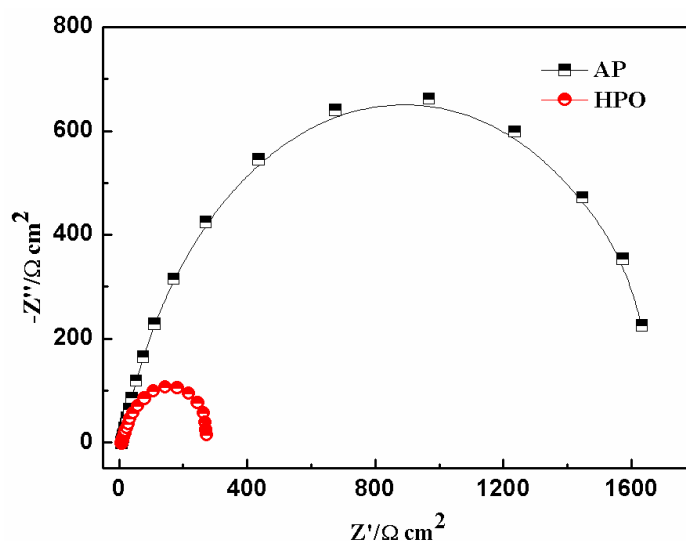


**Figure 13.** EIS plots of low-alloy steel at AP and HPO in neutral 3.5 wt.% NaCl solution.

EIS measurements of low-alloy steel were carried out at AP and HPO in 3.5 wt.% NaCl solution and the results are shown in Fig. 13. The Nyquist plots at AP and HPO are both manifested as a single

semicircle, indicating that the impedance behavior of steel specimens both have one time constant 27. The sizes of the semicircles can be utilized to demonstrate the charge-transfer resistance of the interface 29. In general, bigger semicircle means better resistance to corrosion attack. Obviously, the size of Nyquist plot at HPO is smaller than that at AP, indicating the acceleration to charge transfer process by HPO.

According to the impedance spectrum features of low-alloy steel, an equivalent circuit (Fig. 14) with a time constant is used for fitting EIS results, where  $R_s$  is the solution resistance,  $R_{ct}$  is the charge transfer resistance of the double-layer capacitor, and a constant phase element (CPE) is used to fit the depressed semicircles.

The fitted results using ZsimpWin program are shown in Table 3. In this model, the corrosion process is completely controlled by charge transfer resistance,  $R_{ct}$ , which can be equivalent to the total polarization resistance. The charge transfer resistance  $R_{ct}$  is 1817  $\Omega$  at AP, which is bigger than that at HPO with 296.5  $\Omega$ . It indicates that the corrosion process is accelerated by HPO.

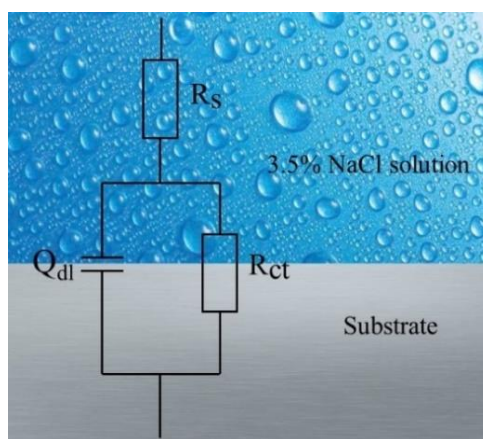


**Figure 14.** Equivalent electrical circuit for EIS data fitting.

**Table 3.** Electrochemical corrosion parameters of low-alloy steel specimens in neutral 3.5 wt.% NaCl solution.

Condition	Time (h)	$R_s$ ( $\Omega \text{ cm}^2$ )	$Q_{dl}$ ( $\mu\Omega \text{ cm}^{-2} \text{ s}^n$ )	$N$	$R_{ct}$ ( $\Omega \text{ cm}^2$ )
AP	1	8.27	807.1	0.78	1817
HPO	1	8.39	650.2	0.76	296.5

### 3.5 Initial potential energy calculation

The results of the electrochemical measurements illustrate that the combined factors of hydrostatic pressure and dissolved oxygen increase the volume of pit formed on low-alloy steel due to the accelerated corrosion process which is mainly contributed by dissolved oxygen. According to the analysis above, the pitting sizes in the horizontal direction relate with dissolved oxygen. Hence, it can be speculated that the dissolved oxygen must change some other factors. To figure out the effect of dissolved oxygen on the pitting growth in the horizontal direction under hydrostatic pressure, the

morphology evolution of a pit at AP was in-situ captured, as presented in Fig. 15. As the steel is immersed in NaCl solution, the pit initiates and propagates at a high rate in the horizontal direction, then stops its propagation after 400s. Afterwards, it grows in the depth direction, which can be seen from the increased corrosion products after 1600s immersion. It reveals that the propagation of pits in the horizontal direction occurs at the very beginning of immersion process. It is considered that pitting initiation is associated with the potential difference at initiation site. But in other opinion, pitting growth can be seen as the transform process from chemical energy to electrical energy. As a result, the propagation of pit in the horizontal direction might be affected by the original surface energy of steel.

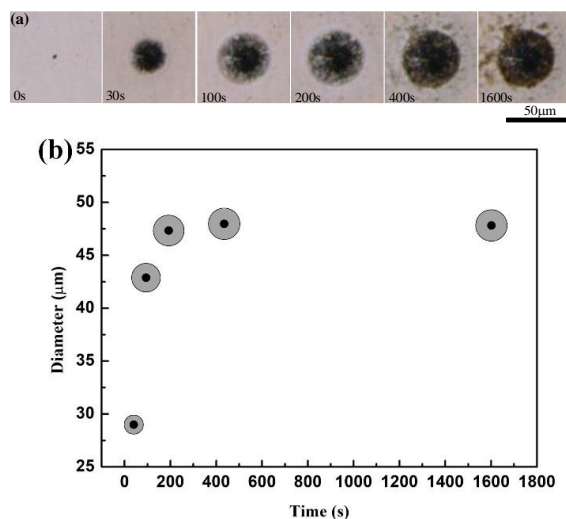
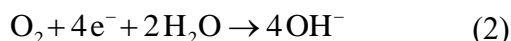


**Figure 15.** Times evolution of pit propagation for low-alloy steel at ordinary pressure in neutral 3.5 wt.% NaCl solution: (a) morphologies, (b) diameters.

SEM morphologies of the corrosion pits for low-alloy steel show that pits initiate at the interface of matrix and inclusion. Zhou et al. and Ke et al. declared that there is a transition region between steel and inclusion which is contaminated by the element from inclusion 34. This transition region has a higher dissolved activity and has a lower potential than the matrix and the inclusion. Here, we assume that the transition region has a homogeneous chemical composition and a uniform dissolved activity. The transition region is served as anode and the reaction is displayed as the following:



The surrounding matrix and inclusion are both served as cathode and the reaction can be shown as the following:



The typical potential distribution for low-alloy steel at initiation site in NaCl solution is illustrated in Fig. 16. Here, it should be noted that the actual potential curve might be a peak-like curve. To simplify calculation, a ladder-shaped curve is used to present the potential distribution. From the view of energy, pitting corrosion can be seen as an ongoing process of eliminating energy difference at the initiation sites, and the absolute value of energy difference can be determined by the respective dissolved activity at different surface areas in NaCl solution.

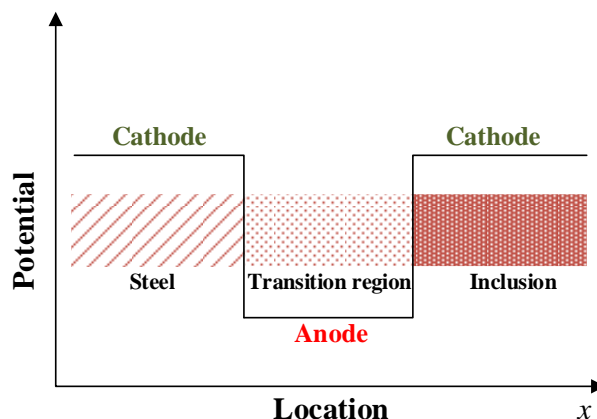


Figure 16. The typical potential distribution at pitting initiation site for low-alloy steel.

If we regard the outmost atom layer of transition region as a capacitance, the energy stored by capacitance can be equal to surface energy difference between anode and cathode. The electrochemical process of pitting corrosion can be seen as a capacitance discharge circuit and pitting growth can be seen as the discharge process of capacitance, as shown in Fig. 17. Then the charge density of capacitance is positively related with the surface charge generating rate of anode (relative dissolved activity) and negatively related with its consumption rate (reaction rate with O<sub>2</sub>).

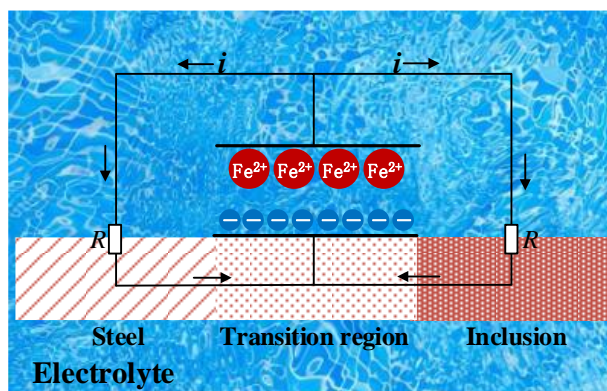


Figure 17. Supposed capacitance discharge circuit at pitting initiation site for low-alloy steel .

The energy stored by capacitance can be seen as the initial potential energy difference between anode (transition region) and cathode (matrix and inclusion) and the initial growth of pits can be regarded as the discharge process of capacitance. The cathode potential at atmospheric environment is given by:

$$E_c = E_{OH^-/O_2}^\ominus + \frac{RT}{zF} \ln \frac{kP_{O_2}}{a_{OH^-}} \tag{3}$$

Where  $E_{OH^-/O_2}^\ominus$  is the standard equilibrium potential;  $R$  is gas constant;  $T$  is the absolute temperature;  $F$  is the Faraday’s constant;  $k$  is a constant,  $P_{O_2}$  is the oxygen partial pressure,  $a_{OH^-}$  is the chemical activity of OH<sup>-</sup>,  $z$  is the number of electrons in the half-reaction.

As the pressure of solution increases from 1 atm (ordinary pressure) to  $x$  atm by pressurizing air into pressure vessel, the dissolved oxygen concentration is  $x$  times of that at atmospheric environment. The increased dissolved oxygen can accelerate the consuming speed of cathodic surface charge, and the charge density of cathodic surface is the  $1/x$  times as much as that at atmospheric environment. The testing environment at ordinary pressure and 25°C temperature can be seen as the standard test environment. At the same time, the potential energy of anode is considered to be identical in different testing environment because its dissolved activity remains unchanged. Therefore, the initial potential difference at initiation sites can be attributed to the potential energy change of cathode. As the testing condition changes from atmospheric environment to the environment containing high hydrostatic pressure and high dissolved oxygen, the potential energy change of cathode is given by:

$$\Delta\varepsilon = \frac{1}{x}q_c E_c^{hp} - q_c E_c^{at} = 0.401q_c \left( \frac{1}{x} + \frac{0.0368 \ln x}{x} - 1 \right) \quad (4)$$

Where  $E_c^{hp}$  is cathodic potential at high hydrostatic pressure and high dissolved oxygen,  $E_c^{at}$  is the cathodic at ordinary pressure. When  $x=1$ ,  $\Delta\varepsilon=0$ ; when  $x>1$ ,  $\Delta\varepsilon > 0$  ( $q_c$  is negative).

Therefore, it can be known that the combined factors of hydrostatic pressure and dissolved oxygen can lower the initial potential energy difference at initiation sites but enhance its potential difference. A lower potential energy difference preferentially triggers a pit with a smaller size in the horizontal direction. Hence, it is believed that the propagation of pits in the horizontal direction is mainly affected by the initial potential energy difference. To demonstrate the reasonability of this opinion, we try to used it to illustrate the effect of hydrostatic pressure on the pitting sizes in the horizontal direction for low-alloy steel.

According to Gutman's mechanistic theory, the change of potential,  $\nabla\varphi$ , on the metal surface is associated with the pressure  $\Delta P$ , which is given by:

$$\nabla\varphi = -\frac{\Delta P V_m}{zF} \quad (5)$$

Where  $\Delta P$  is external pressure,  $V_m$  is the molar volume of the matrix,  $z$  is the valence of the element, and  $F$  is the Faraday constant.

From equation (5), it can be known that hydrostatic pressure can reduce surface potential of steel. The anode potential decreases with the increase of hydrostatic pressure while the cathode potential maintains constant due to the unchanged dissolved oxygen concentration. Then hydrostatic pressure can accelerate the dissolved activity of Fe matrix and increase the generating rate of charge at the transition region due to the increase of  $Cl^-$  activity. Hence, hydrostatic pressure also increases the charge density on the surface of transition region. As a result, hydrostatic pressure increases the initial potential energy difference at initiation sites, stimulating the horizontal propagation of pits. This conclusion is consistent with the results of Yang et al. 11 that hydrostatic pressure increases pitting growth in the horizontal direction and stimulates the coalescence of nearby pits.

Based on in-situ observation of pitting morphology evolution, the supposed growth kinetics curves for corrosion pits at AP and HPO are presented in Fig. 18. Presumably, the pit initiates on low-alloy steel surface immediately as the steel is immersed in NaCl solution, and then mainly propagates in the horizontal direction at a high rate due to the initial potential energy difference at initiation sites. After

the pit is covered with corrosion products, it grows slowly in the horizontal direction and ceases to grow in this direction after a short period of immersion. Afterwards, the pit grows at a relatively slow rate in the depth direction. HPO decreases the initial potential energy difference at initiation sites and inhibits the pitting growth in the horizontal direction. Nevertheless, HPO reduces the time for pitting growth in the horizontal direction and promotes the pitting growth rate in the depth direction.

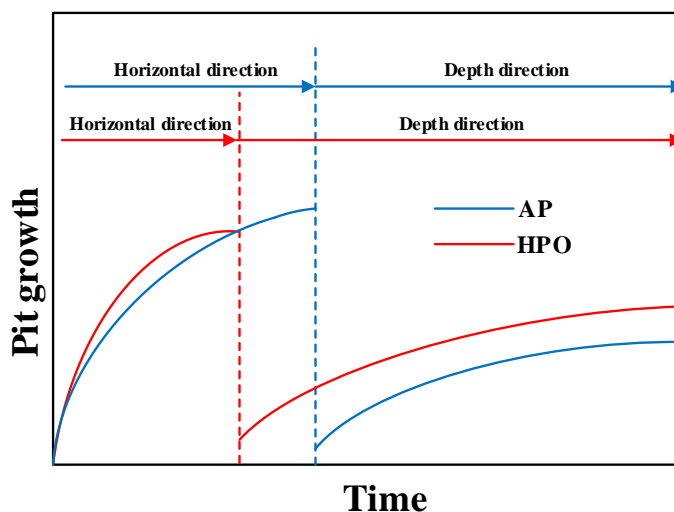


**Figure 18.** Supposed growth kinetics curves for corrosion pits of low-alloy steel at AP and HPO in neutral 3.5 wt.% NaCl solution.

#### 4. CONCLUSIONS

Effect of dissolved oxygen on pitting corrosion of low-alloy steel under hydrostatic pressure was investigated in neutral 3.5 wt.% NaCl solution. The combined effect of hydrostatic pressure and dissolved oxygen increases the depth and volume of corrosion pits, however, decreases their sizes in the horizontal direction. Dissolved oxygen plays a leading role in the corrosion kinetics of low-alloy steel in the environment containing high hydrostatic pressure and high dissolved oxygen. Dissolved oxygen can accelerate cathodic process and inhibit anodic process under hydrostatic pressure, giving an overall result of an increased corrosion rate, therefore, increasing the volume and depth of pits. Meanwhile, dissolved oxygen decreases the potential energy difference at initiation sites of pits under hydrostatic pressure, possibly inhibiting the pitting growth in the horizontal direction.

#### ACKNOWLEDGEMENTS

The authors would like to thank the financial supports from the National Natural Science Foundation of China (Project 51675533, 51701238 and 51705521).

#### References

1. I. Ulanovskii, *Prot. Met.*, 15 (1979) 563.
2. I. Ulanovskii, V. Egorova, *Prot. Met.*, 14 (1978) 137.
3. F. Reinhart, J. Jenkins, "Corrosion of materials in surface seawater after 12 and 18 months"

- Technical Note N-1213, Naval Civil Engineering Laboratory, Port Hueneme, CA, 1972.
4. R. Venkatesan, M. Venkatasamy, T. Bhaskaran, E. Dwarakadasa, *Brit. Corros. J.*, 37 (2002) 257.
  5. S. Sawant, A. Wagh, *Corros. Prevent. Contr.*, 37 (1990) 154.
  6. A.M. Beccaria, G. Poggi, *Brit. Corros. J.*, 20 (1985) 183.
  7. B. Liu, T. Zhang, Y.W. Shao, G.Z. Meng, J.T. Liu, F.H. Wang, *Int. J. Electrochem. Sci.*, 7 (2012) 1864.
  8. C. Zhang, Z.W. Zhang, L. Liu, *Electrochim. Acta*, 210 (2016) 401.
  9. H.J. Sun, L. Liu, Y. Li, F.H. Wang, low-alloy steel *J. Electrochem. Soc.*, 160 (2013) C89.
  10. Y.G. Yang, T. Zhang, Y.W. Shao, G.Z. Meng, F.H. Wang, *Corros. Sci.*, 52 (2010) 2697.
  11. Y.G. Yang, T. Zhang, Y.W. Shao, G.Z. Meng, F.H. Wang, *Corros. Sci.*, 73 (2013) 250.
  12. G.S. Frankel, *J. Electrochem. Soc.*, 145 (1998) 2186.
  13. B. Zhang, J. Wang, B. Wu, Y.T. Zhou, X.L. Ma, *Corros. Sci.*, 100 (2015) 295.
  14. K. Wang, X. Ma, Y. Wang, R. He, *J. Electrochem. Soc.*, 164 (2017) C453.
  15. I. Muto, Y. Izumiyama, N. Hara, *J. Electrochem. Soc.*, 154 (2007) C439.
  16. Z. Ye, Z. Zhu, Q. Zhang, X. Liu, J. Zhang, F. Cao, *Corros. Sci.*, 143 (2018) 221.
  17. D. Kong, C. Dong, Z. Zheng, F. Mao, A. Xu, X. Ni, C. Man, J. Yao, K. Xiao, X. Li, *Appl. Surf. Sci.*, 440 (2018) 245.
  18. D. Zhang, H. Terasaki, Y.I. Komizo, *Acta Mater.*, 58 (2010) 1369.
  19. A. Valor, F. Caleyó, L. Alfonso, D. Rivas, *Corros. Sci.*, 49 (2007) 559.
  20. D.E. Williams, C. Westcott, M. Fleischmann, *J. Electroanal. Chem.*, 180 (1984) 549.
  21. F. Arjmand, L. Zhang, J. Wang, *Nucl. Eng. Des.*, 322 (2017) 215.
  22. Z. Feng, X. Cheng, C. Dong, L. Xu, X. Li, *J. Nucl. Mater.*, 407 (2010) 171.
  23. Y.X. Qiao, Y.G. Zheng, P.C. Okafor, W. Ke, *Electrochim. Acta*, 54 (2009) 2298.
  24. Z. Wang, J. Liu, L. Wu, R. Han, Y. Sun, *Corros. Sci.*, 67 (2013) 1.
  25. T. Nishimura, T. Kodama, *Corros. Sci.*, 45 (2003) 1073.
  26. Y.S. Choi, J.J. Shim, J.G. Kim, *Corrosion*, 61 (2005) 490.
  27. J.J. Shim, J.G. Kim, *Mater. Lett.*, 58 (2004) 2002.
  28. S. Ahn, H. Kwon, D.D. Macdonald, *J. Electrochem. Soc.*, 152 (2005) B482.
  29. H.S. Klapper, J. Goellner, A. Burkert, A. Heyn, *Corros. Sci.*, 75 (2013) 239.
  30. J. Han, J.W. Carey, J. Zhang, *J. Appl. Electrochem.*, 41 (2011) 741.
  31. I.L. Muller, J.R. Galvele, *Corros. Sci.*, 17 (1977) 995.
  32. J. Srinivasan, R.G. Kelly, *Corrosion*, 70 (2014) 1172.
  33. T. Suter, E.G. Webb, H. Bohni, R.C. Alkire, *J. Electrochem. Soc.*, 148 (2001) B174.
  34. Y.T. Zhou, S.J. Zheng, B. Zhang, X.L. Ma, *Corros. Sci.*, 111 (2016) 414.
  35. R. Ke, J.E. Castle, *Corros. Sci.*, 30 (1990) 409.
  36. D.E. Williams, M.R. Kilburn, J. Cliff, G.I.N. Waterhouse, *Corros. Sci.*, 52 (2010) 3702.
  37. V. Maurice, G. Despert, S. Zanna, M.P. Bacos, P. Marcus, *Nat. Mater.*, 3 (2004) 687.
  38. P. Schmuki, H. Hildebrand, A. Friedrich, S. Virtanen, *Corros. Sci.*, 47 (2005) 1239.
  39. G. Wranglén, *Corros. Sci.*, 14 (1974) 331.
  40. L.Y. Xu, Y.F. Cheng, *Corros. Sci.*, 59 (2012) 103.
  41. L.Y. Xu, Y.F. Cheng, *Corros. Sci.*, 64 (2012) 145.
  42. Y. Wang, W. Zhao, H. Ai, X. Zhou, T. Zhang, *Corros. Sci.*, 53 (2011) 2761.